

# A Study of the Gamma-Ray Burst Fundamental Plane

Dainotti, M. G. <sup>1,2,3</sup>, Hernandez, X. <sup>4</sup>, Postnikov, S. <sup>5</sup>, Nagataki, S. <sup>6</sup>, O'brien, P <sup>7</sup>, Willingale, R. <sup>7</sup>, S. Striegel <sup>8</sup>

September 2, 2022

## ABSTRACT

Long gamma-ray bursts (GRBs) with a plateau phase in their X-ray afterglows obeys a three-dimensional (3D) relation (Dainotti et al. 2016), between the rest-frame time at the end of the plateau,  $T_a$ , its corresponding X-ray luminosity,  $L_a$ , and the peak luminosity in the prompt emission,  $L_{peak}$ . This 3D relation identifies a GRB fundamental plane whose existence we here confirm. Here, we include the most recent GRBs observed by Swift to define a ‘gold sample’ (45 GRBs) and obtain an intrinsic scatter about the plane compatible within one  $\sigma$  with the previous result. We compare GRB categories, such as short with extended emission, SEE, X-ray Flashes, GRBs associated with SNe, a sample of only long-duration GRBs (132), selected from the total sample by excluding GRBs of the previous categories, and the gold sample, composed by GRBs with lightcurves with good data coverage and relatively flat plateaus. We find that the relation planes for each of these categories are not statistically different from the

---

<sup>1</sup>Department of Physics & Astronomy, Stanford University, Via Pueblo Mall 382, Stanford, CA 94305-4060, USA; mdainott@stanford.edu

<sup>2</sup>Obserwatorium Astronomiczne, Uniwersytet Jagielloński, ul. Orla 171, 31-501 Kraków, Poland; dainotti@oa.uj.edu.pl

<sup>3</sup>INAF-Istituto di Astrofísica Spaziale e Física cosmica, c/o CNR - Area della Ricerca di Bologna, Via Gobetti 101, I-40129 - Bologna, Italy; mariagiovannadainotti@yahoo.it

<sup>4</sup>Instituto de Astronomía, Universidad Nacional Autónoma de México, Ciudad de México 04510, México  
E-mail: xavier@astro.unam.mx

<sup>5</sup>The Center for Exploration of Energy and Matter, Indiana University, Bloomington, IN 47405, USA; postsergey@gmail.com

<sup>6</sup>RIKEN, Hirosawa, Wako Saitama, Japan; shigehiro.nagataki@riken.jp

<sup>7</sup>Department of Physics & Astronomy, University of Leicester, Road Leicester LE1 7RH, UK; zrw@le.ac.uk

<sup>8</sup>Department of Physics & Astronomy, San Jose State University, One Washington Square, San Jose, CA 95192, USA; stephanie.striegel@sjsu.edu

gold fundamental plane, with the exception of the SSE, which are hence identified as a physically distinct class. The gold fundamental plane has an intrinsic scatter smaller than any plane derived from the other sample categories. Thus, the distance of any particular GRB category from this plane becomes a key parameter. We computed the several category planes with  $T_a$  as a dependent parameter obtaining for each category smaller intrinsic scatters (reaching a reduction of 24% for the long GRBs). The fundamental plane is independent from several prompt and afterglow parameters.

*Subject headings:* gamma-rays bursts: general - methods: statistical

## 1. Introduction

Gamma-ray bursts (GRBs) have typical isotropic prompt emission energies,  $E_{iso}$ , in the range of  $10^{53}$  erg, and thus can be observed up to redshifts,  $z$ , of  $\sim 10$  (Cucchiara et al. 2011). This last feature raises the tantalizing possibility of extending direct cosmological studies far beyond the redshift range covered by supernovae (SNe). However, GRBs are not simple standard candles, as their intrinsic energies span several orders of magnitude. The variety of their features makes it extremely difficult to categorize them under certain common patterns. Indeed, the number of sub-classes into which GRBs are grouped has grown since their discovery. GRBs are traditionally classified depending on their duration into short ( $T_{90} \leq 2$  s) and long ( $T_{90} \geq 2$  s)<sup>1</sup> (Mazets et al. 1981; Kouveliotou et al. 1993). Later, a class of GRBs with mixed properties, such as short GRBs with extended emission (SEE), was discovered (Norris & Bonnell 2006). Long GRBs, depending on their fluence (erg cm<sup>-2</sup>), can be divided into normal GRBs or X-ray Flashes (XRFs); the latter are empirically defined as GRBs with a greater fluence in the X-ray band (2–30 keV) than in the  $\gamma$ -ray band (30–400 keV). In addition, several GRBs also present associated SNe; hereafter they are referred to as GRB-SNe. Recently, a new category of ultra-long GRBs has been discovered (Levan et al. 2014). These GRBs present remarkably unusual X-ray and optical lightcurves, very different from classical GRBs, with long lasting highly variable X-ray emission, and optical lightcurves showing a weak correlation with the behaviour seen in the X-ray. Levan et al. (2014) proposed that these bursts, difficult to detect, are the first examples of a new population of ultra-long GRBs, that may be astrophysically relatively common. The long durations may be explained by the engine-driven explosions of stars of much larger radii than those that are usually considered as

---

<sup>1</sup>where  $T_{90}$  is the time interval over which between 5% and 95% of the total prompt energy is emitted.

GRB progenitors, which are thought to have compact Wolf-Rayet progenitor stars. However, Levan et al. (2014) claimed that it is not possible to unequivocally identify supernova signatures within their lightcurves or spectra. Thus, they also considered that they may arise from the tidal disruption of stars by supermassive black holes. Other ultra-long GRBs have been observed, for example GRB 130925A, to have features which are associated with a low metallicity blue supergiant progenitor and could characterize the class of ultra-long GRBs (Piro et al. 2014).

Regarding lightcurve morphology, a more complex trend in the afterglow has been observed with the *Swift* Satellite<sup>(Gehrels et al. 2004; O’ Brien et al. 2006)</sup> compared to previous missions. Due to *Swift*, it has been discovered that there is a flat part, the plateau, of GRB lightcurves soon after the steep decay of the prompt emission. Along with these categories, several physical mechanisms for producing GRBs have also been proposed. For example, the plateau emission has mainly been ascribed to millisecond newborn spinning neutron stars, (e.g., Zhang & Mészáros 2001; Troja et al. 2007; Dall’Osso et al. 2011; Rowlinson et al. 2013, 2014; Rea et al. 2015) or to accretion onto a black hole (Cannizzo & Gerhels 2009; Cannizzo et al. 2011). A very promising field has been the hunt for correlations between physically meaningful GRB parameters, (e.g., Amati et al. 2002; Yonetoku et al. 2004; Ghirlanda et al. 2004; Ghisellini et al. 2008; Oates et al. 2009, 2012; Qi et al. 2009; Willingale et al. 2010), in order to employ GRBs as cosmological indicators, as cosmological tools and as theoretical model discriminators.

The relations discovered so far suffer from having large scatters (Collazzi & Schaefer 2008), beyond observational uncertainties, highlighting that the events studied probably come from different classes of systems or perhaps from the same class of objects, but we do not yet observe a sufficiently large number of parameters to characterize the scatter. Indeed, other possible sources of scatter about relations could depend on the difference in bulk Lorenz factor, in the density of the medium that can be homogeneous or of a stellar wind type, in the viewing angles etc. In addition, the majority of such relations consider the GRB emission as isotropic, but a small jet opening is also possible. The jet opening angle is very difficult to infer due to the paucity of multi-wavelength observations. Several methods have been proposed in the literature to obtain an independent estimate of the jet opening angle (Ghirlanda et al. 2004; Lu et al. 2012; Fong et al. 2015; Goldstein et al. 2016).

As was pointed out in Dainotti et al. (2010), in order to properly use GRB relations as reliable model discriminators and cosmological tools, it is necessary to define type specific GRB categories to yield a more homogeneous, observationally-motivated sample. In fact, it may be that the scatter of the GRB scaling relations could be partly explained by the mixing of GRBs with different intrinsic physics. Isolating GRB categories allows us to derive tighter

relations, thus, increasing the accuracy with which cosmological parameters are inferred (e.g., Cardone et al. 2009, 2010; Dainotti et al. 2013b; Postnikov et al. 2014).

One of the first attempts to standardize GRBs in the afterglow parameters was presented with the Dainotti relation (Dainotti et al. 2008, Dainotti et al. 2010), where an approximately inversely proportional law between the rest-frame time at the end of the plateau phase,  $T_a$  (in previous papers  $T_a^*$ ), and its corresponding luminosity,  $L_a$ , was discovered. Dainotti et al. (2013a) proved through the robust statistical Efron & Petrosian (1992) method, hereafter EP, that this correlation is intrinsic, and not an artifact of selection effects or due to instrumental threshold truncation, as is also the case for the  $L_{peak} - L_a$  relation (Dainotti et al. 2011b, 2015b), where  $L_{peak}$  is the 1s peak luminosity in the prompt emission.

In this paper we use a large GRB sample to confirm results discussed in Dainotti et al. (2016), namely, that the peculiar plateau phase in GRBs can be employed to isolate a sub-class of events that define a very tight plane in a three-dimensional space of  $(\log L_a, \log T_a, \log L_{peak})$ . Results of this paper have been presented in a NASA press release<sup>2</sup> at the 228th AAS Meeting. We here confirm that the scatter about the fundamental plane is the smallest for the gold sample, a specific class of GRBs without steep plateaus and with good data coverage when we consider  $L_a$  as the independent variable. We have extended the previous gold sample to 45 GRBs obtaining an intrinsic scatter compatible with our previous finding to within one  $\sigma$ . We find that other relation planes for the different categories have larger scatter than the fundamental plane derived from the gold sample. We also show that the fundamental plane is independent from several prompt and afterglow parameters, such as the rest frame prompt emission duration,  $\frac{T_{90}}{(1+z)} = T_{90}^*$ , rest frame peak energy,  $E_{peak} * (1+z) = E_{peak}^*$ , the temporal decay index after the plateau emission,  $\alpha$  and the jet opening angle,  $\theta_{jet}$ . Thus, we can conclude that the plane is stable and not in fact a hypersurface in four dimensions. This analysis is relevant, because it shows the robustness of the fundamental plane and hence we can possibly use it in future as a cosmological tool due to its small scatter. We note that we have already addressed for both the  $L_X - T_a^*$  and the  $L_{peak} - T_a^*$  relations their cosmological evolutions and determined their intrinsic correlations. This paper also constitutes an update and presents a new investigation with respect to the previous analysis presented in Dainotti et al. (2016a), as the validity of our conclusion have been extended by including a high energy subsample of GRBs observed by the Fermi-GBM (Gamma Ray Burst Monitor). We also test a plane for which the variable  $T_a$  is a function of  $L_{peak}$  and  $L_a$ . The choice of  $T_a$  as a dependent variable reduces the intrinsic scatter of the all long GRBs by a further 24%. In addition, we show that the distance to the

---

<sup>2</sup>[https://swift.gsfc.nasa.gov/news/2016/grbs\\_std\\_candles.html](https://swift.gsfc.nasa.gov/news/2016/grbs_std_candles.html)

gold sample fundamental plane can be considered as a new key parameter to discriminate among long and SEE bursts. In Sections §2 and §3 we describe the *Swift* data samples used and the three-parameter relations for those samples, respectively. In section §4 we present the independence of the  $(L_a, T_a, L_{peak})$  relation from other relevant prompt and afterglow parameters. In §5, we summarize our findings and conclusions.

## 2. Sample Selection

We analyzed 183 GRB X-ray plateau afterglows detected by *Swift* from 2005 January up to 2016 July with known redshifts, spectroscopic or photometric, available in Xiao & Schaefer (2009), on the Greiner webpage<sup>3</sup> and in the Gamma-ray Coordinates Network (GCN) circulairs and notices<sup>4</sup>, excluding redshifts for which there is only a lower or an upper limit. The redshift range of our sample is (0.033, 9.4). We include all GRBs for which the Burst Alert Telescope (BAT) + X-Ray Telescope (XRT) lightcurves can be fitted by the phenomenological Willingale et al. (2007) model (hereafter W07). The W07 functional form for  $f(t)$  is:

$$f(t) = \begin{cases} F_i \exp\left(\alpha_i\left(1 - \frac{t}{T_i}\right)\right) \exp\left(-\frac{t_i}{t}\right) & \text{for } t < T_i \\ F_i \left(\frac{t}{T_i}\right)^{-\alpha_i} \exp\left(-\frac{t_i}{t}\right) & \text{for } t \geq T_i \end{cases} \quad (1)$$

for both the prompt (index “i=p”)  $\gamma$ -ray and initial X-ray decay and for the afterglow (“i=a”), modeled so that the complete lightcurve  $f_{tot}(t) = f_p(t) + f_a(t)$  contains two sets of four free parameters ( $T_i, F_i, \alpha_i, t_i$ ). The transition from the exponential to the power law (PL) occurs at the point  $(T_i, F_i e^{-t_i/T_i})$  where the two functional forms have the same value. The parameter  $\alpha_i$  is the temporal PL decay index and the time  $t_i$  is the initial rise timescale. We exclude the cases when the fitting procedure fails or when the determination of  $1\sigma$  confidence intervals does not fulfill the Avni (1976)  $\chi^2$  prescriptions, see the XSPEC manual<sup>5</sup>. Thus, we ended up with a sample of 183 GRBs. We compute the source rest-frame isotropic luminosity

---

<sup>3</sup><http://www.mpe.mpg.de/jcg/grbgen.html>

<sup>4</sup><http://gcn.gsfc.nasa.gov/>

<sup>5</sup><http://heasarc.nasa.gov/xanadu/xspec/manual/XspecSpectralFitting.html>

$L_a$  in units of  $\text{erg s}^{-1}$  in the *Swift* XRT bandpass,  $(E_{min}, E_{max}) = (0.3, 10) \text{ keV}$  as follows:

$$L_a = 4\pi D_L^2(z) F_X(E_{min}, E_{max}, T_a) \cdot K, \quad (2)$$

where  $D_L(z)$  is the luminosity distance for the redshift  $z$ , assuming a flat  $\Lambda\text{CDM}$  cosmological model with  $\Omega_M = 0.3$  and  $H_0 = 70 \text{ km s}^{-1} \text{Mpc}^{-1}$ ,  $F_X$  is the measured X-ray energy flux in  $(\text{erg cm}^{-2} \text{s}^{-1})$ , and  $K$  is the  $K$ -correction for cosmic expansion. For *Swift* GRBs, the  $K$ -correction is simply  $(1+z)^{(\beta-1)}$ , where  $\beta$  is the X-ray spectral index of the plateau phase. For *Fermi* GRBs, the  $K$ -correction is the solution of this integral:

$$\frac{\int_{\frac{100}{(1+z)}}^{\frac{1000}{(1+z)}} N(E)}{\int_{100}^{1000} N(E)}, \quad (3)$$

where  $N(E)$  is the functional form of the spectrum, represented either by a CPL or a Band function. We here note that the luminosity is calculated for both  $L_{peak}$  and  $L_a$  in a consistent rest-frame band, which is the Swift-BAT, XRT and the Fermi-GBM bands, for each GRB and hence such a luminosity computation does not lead to any induced correlation. We downloaded the lightcurves from the Swift webpage repository<sup>6</sup> and we derived the spectral parameters following Evans et al. (2009). As shown in Dainotti et al. (2010), requiring an observationally homogeneous sample in terms of  $T_{90}^*$  and spectral lag properties implies removing short GRBs ( $T_{90} \leq 2 \text{ s}$ ) and SEE from the analysis. We separated the GRBs cataloged as SEE in Norris & Bonnel (2006), Levan et al. (2007), Norris et al. (2010). For the evaluation of the remaining SEE GRBs we follow the definition of Norris et al. (2010), who identify SEE events as those presenting short spikes followed, within 10 s, by a decrease in the intensity emission by a factor of  $10^3$  to  $10^2$ , but with almost negligible spectral lag. Moreover, because there are long GRBs for which an associated SNe has not been detected, such as, for example the nearby  $z = 0.09$  SNe-less GRB 060505, the existence of a new group of long GRBs without SNe has been suggested, thus highlighting the possibility of two types of long GRBs, with and without SNe. Therefore, in the interest of selecting an observational homogeneous class of objects, we segregate long GRBs with no associated SNe from the other categories. Under this specific criterion all the GRB-SNe that follow the Hjorth & Bloom (2011) classification are considered separately. Within the GRB-SNe sample, we applied a further classification, which is an update of the one of Hjorth & Bloom (2011). This identifies GRB-SNe sub-samples based on the quality of the identification of

---

<sup>6</sup>[http://www.swift.ac.uk/burst\\_analyser](http://www.swift.ac.uk/burst_analyser)

SNe associated to the GRB. The categories considered are: A) strong spectroscopic evidence for a SN associated with the GRB, B) a clear lightcurve bump as well as some spectroscopic evidence suggesting the LONG-SNe association, C) a clear bump on the lightcurve consistent with the GRB-SNe association, but no spectroscopic evidence of the SN, D) a significant bump on the lightcurve, but the inferred SN properties are not fully consistent with other GRB-SNe associations or the bump is not well sampled or there is no spectroscopic redshift of the GRB, E) a bump, either of low significance or inconsistent with other observed GRB-SNe identifications, but with a spectroscopic redshift of the GRB. Similarly, to evaluate samples which are homogeneous regarding the ratio between  $\gamma$ -ray and X-ray fluence, we separated all XRFs from the other mentioned categories. The selection criteria are applied in the observer frame.

In all that follows,  $L_{peak}$  ( $erg\ s^{-1}$ ) is defined as the prompt emission peak luminosity over a 1 s interval. Following Schaefer (2007) we compute  $L_{peak}$  as follows:

$$L_{peak} = 4\pi D_L^2(z) F_{peak}(E_{min}, E_{max}, T_a) \cdot K, \quad (4)$$

where  $F_{peak}$  is the measured gamma-ray energy flux over a 1 s interval ( $erg\ cm^{-2}s^{-1}$ ). To further create a sample with more homogeneous spectral features, we consider only the GRBs for which the spectrum computed at 1 s has a smaller  $\chi^2$  for a single PL fit than for a cutoff power law (CPL). Specifically, following Sakamoto et al. (2010), when the  $\chi^2_{CPL} - \chi^2_{PL} < 6$ , the PL fit is preferred. In addition, for all GRBs that satisfy this criterion there is not a substantial difference in spectral fitting results if one considers either a PL or a CPL.

As we have already anticipated in the introduction, the plane is confirmed also for GRBs observed by the Fermi-GBM. We consider a subsample of 76 GRBs, which are observed to have a plateau and are detected by both the Fermi/GBM and Swift. Of these 76 GRBs, we have selected 47 GRBs using the following selection criteria:  $\delta_{F_{peak}}/F_{peak} \leq 1$ ,  $\delta_\alpha/\alpha \leq 1$ ,  $\delta_\beta/\beta \leq 1$  (where  $\alpha$  and  $\beta$  are the spectral parameters for high energy and lower energy tail for the Band function). This guarantees not only that the errors in the determined parameters are smaller than the parameters themselves, but also that these results are robust and independent of the instrument selected to measure the peak flux in the prompt emission. Among these 47 GRBs, 34 are long, 13 are gold, 3 are SSE, 5 are GRB-SNe associated and 5 are XRFs. We note that  $L_{peak}$  is computed from  $F_{peak}$  which has been binned at 1024 ms. The choice of the prompt peak luminosity as a third parameter guarantees that there is no contamination from the early afterglow and thus the correlation with the afterglow luminosity is intrinsic. A confirmation of this statement comes from the use of peak luminosity computed in the 10 – 1000 keV Fermi band, a much larger energy range compared to the Swift-BAT range (15 – 150 keV). For the GRBs observed by Swift we additionally discard 6 GRBs that

were better fitted with a blackbody model than with a PL. This full set of requirements reduces the sample to 132 long GRBs. Finally, we construct a sub-sample by including strict data quality and the following morphology requirements: the beginning of the plateau should have at least five data points and the plateau should not be too steep (the angle of the plateau must be less than  $41^\circ$ )<sup>7</sup>. The first of the above selection rules guarantees that the lightcurves clearly present the transition from the steep decay after the prompt emission to the plateau phase. The number of points required for the W07 fit should be at least four, since there are four free parameters in the model, one of which should be after the end of the plateau. Thus, the requirement of six points in total (five at the start and at least one after the plateau) ensures a minimum number of points to have both a clear transition to the plateau phase and simultaneously to constrain the plateau. This data quality criterion defines the gold sample which includes 45 GRBs. We have also confirmed through the  $T$ -test that this gold sample is not statistically different in terms of  $(L_a, T_a, L_{peak}, z)$  distribution from the full sample, thus showing that the choice of this sample does not introduce any biases, such as the Malmquist or Eddington ones, against high luminosity and/or high redshift GRBs. Specifically,  $L_a, T_a, L_{peak}$  and  $z$  for the gold sample present similar Gaussian distributions, but with smaller tails than the total sample (see Dainotti et al. 2015a); thus there is no shift of the distribution toward high luminosities, larger times, or high redshift. Hence, the selection cut naturally removes the majority of the high error outliers of the variables involved, thus reducing the scatter of the relation for the gold sample.

We analyzed separately from the gold sample the following GRB categories: SEE (Norris & Bonnel 2006; Levan et al. 2007; Norris et al. 2010), the complete GRB-SNe sample (Hjorth & Bloom 2011), the sub-sample of GRBs spectroscopically associated with SNe (classifications A, B, and C from Hjorth & Bloom 2011), XRFs, and long GRBs excluded from the ultra-long GRB category and the previous categories.

### 3. The 3D Relation for Long GRBs, XRF, SEE, GRB-SNe, and the Gold Sample

Figure (1) shows all 183 GRBs in the  $(L_a, T_a, L_{peak})$  parameter space, divided into five categories: GRB-SNe (cones), X-ray flashes (spheres), SEE (cuboids), long GRBs (circles), and ultra-long GRBs (polyhedrons). Darker colors indicate data points above the plane,

---

<sup>7</sup>The angle of the plateau is obtained using trigonometry as the difference between the fluxes,  $\Delta_F = F_i - F_a$ , where  $i$  is the time of the beginning of the plateau emission divided by the difference between  $\delta_T = T_a - T_i$ .

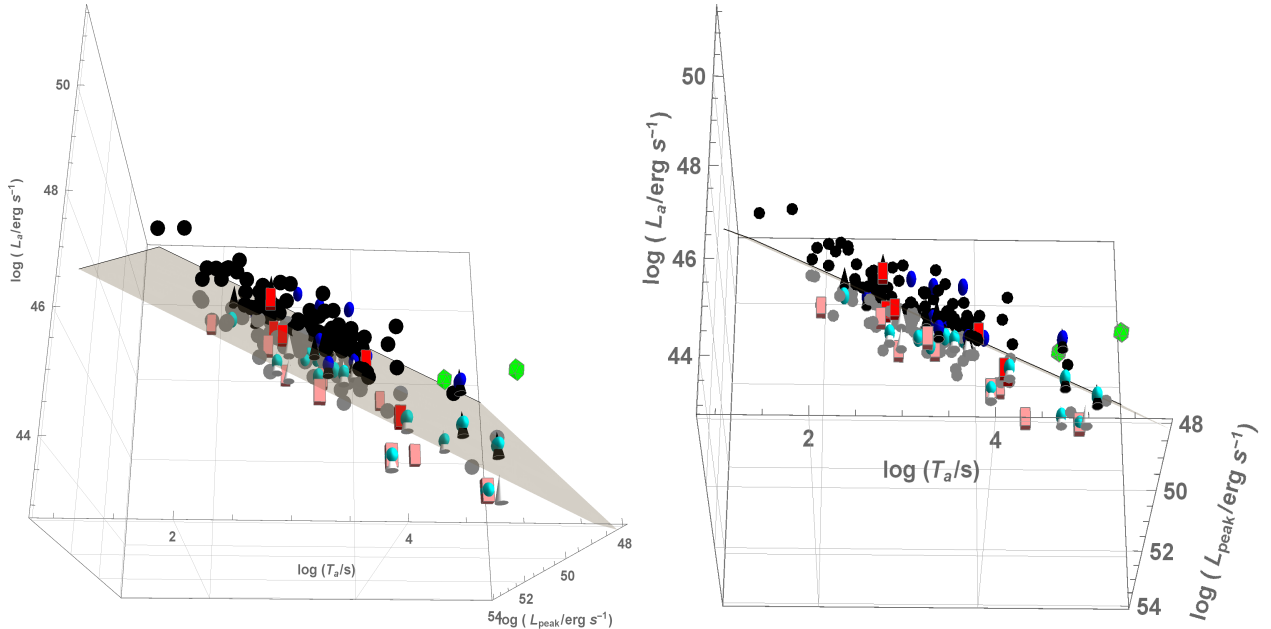


Fig. 1.— Left panel: 183 GRBs in the  $(L_a, T_a, L_{peak})$  space, with a plane fitted using the 183 GRBs, including GRB-SNe (cones), X-ray flashes (spheres), SEE (cuboids), long GRBs (circles), and ultra-long GRBs (polyhedrons). Darker colors indicate data points above the plane, while lighter colors indicate data points below the plane. This figure shows one of the possible projections. Right panel: the same data are shown, but for an edge on projection.

while lighter colors indicate data points below the plane. It can be noted that the separate sub-classes of GRBs show greater spread about the plane than the long GRB sample. Using the method described in Dainotti et al. (2016), we use the parameters  $L_a$ ,  $T_a$ , and  $L_{peak}$  to create a best-fit plane for the GRB categories. When we parametrize this plane using the angles  $\theta$  and  $\phi$  of its unit normal vector, the following formula is used:

$$\log L_a = C_o - \cos(\phi) \tan(\theta) \log T_a - \sin(\phi) \tan(\theta) \log L_{peak} \quad (5)$$

where  $C_o = C(\theta, \phi, \sigma_{int}) + z_o$  is the normalization of the plane correlated with the other variables,  $\theta$ ,  $\phi$  and  $\sigma_{int}$ ; while  $z_o$  is an uncorrelated fitting parameter related to the normalization and  $C$  is the covariance function. For simplicity, we will rewrite the previous formula in the following way:

$$\log L_a = C_o + a \times \log T_a + b \times \log L_{peak} \quad (6)$$

where  $a(\theta, \phi) = -\cos(\phi) \tan(\theta)$  and  $b(\theta, \phi) = -\sin(\phi) \tan(\theta)$ . This normalization of the plane allows the resulting parameter set,  $\theta$ ,  $\phi$ ,  $\sigma_{int}$  and  $z_o$  to be uncorrelated and provides explicit error propagation. For example, with the updated gold sample, we obtain a new optimal plane:

$$\log L_a = (17.65 \pm 5.7) - (0.83 \pm 0.10) \log T_a + (0.64 \pm 0.11) \log L_{peak}, \quad (7)$$

where  $C_o = (17.65 \pm 5.7)$ ,  $a = -(0.83 \pm 0.10)$  and  $b = (0.64 \pm 0.11)$ . All of the fits shown in this paper were performed using the D'Agostini method<sup>(D'Agostini 2005)</sup>. Uncertainties are always given as  $1\sigma$ .

For the updated gold plane  $\sigma_{int} = 0.316 \pm 0.039$ , which is within  $1\sigma$  of the previously obtained value of  $\sigma_{int} = 0.27 \pm 0.04$ . The  $R_{adj}^2$  for the gold sample has slightly increased from 0.8 to 0.81, but remains comparable to the original gold sample.  $R_{adj}^2$  gives a version of the coefficient of determination,  $R^2$ , which is adjusted for the number of parameters in the model. The Pearson correlation coefficient,  $r$ , is 0.90 with a probability of the same sample occurring by chance,  $P = 1.75 \times 10^{-17}$ . The normalization of the plane,  $C(\sigma_{int}, \phi, \theta)$ , is given by:

$$C = 13.90 - 62.28\theta^2 - 0.29\sigma_{int} + 0.38\sigma_{int}^2 - 8.23\phi - 0.05\sigma_{int}\phi + 15.13\phi^2 + \theta(99.62 - 0.10\sigma_{int} + 90.31\phi). \quad (8)$$

Category	$C_o$	a	b	$\sigma_{int}$	N
Gold	$17.65 \pm 5.68$	$-0.83 \pm 0.1$	$0.64 \pm 0.11$	$0.32 \pm 0.04$	45
SNe ABC	$20.87 \pm 6.5$	$-1.03 \pm 0.12$	$0.58 \pm 0.13$	$0.33 \pm 0.08$	11
SEE	$14.11 \pm 8.16$	$-1.05 \pm 0.14$	$0.71 \pm 0.16$	$0.39 \pm 0.09$	15
Long	$14.52 \pm 3.67$	$-0.87 \pm 0.06$	$0.7 \pm 0.07$	$0.41 \pm 0.03$	132
SNe Total	$10.19 \pm 6.55$	$-0.78 \pm 0.12$	$0.77 \pm 0.13$	$0.5 \pm 0.08$	22
XRF	$9.03 \pm 7.14$	$-0.71 \pm 0.14$	$0.79 \pm 0.13$	$0.53 \pm 0.08$	27

Table 1: Table of best-fit values for relation plane parameters in order of increasing scatter,  $\sigma_{int}$ .

The correlation was also calculated for all of the mentioned GRB sub-classes. The values for these fits are shown in Table (1) which shows sub-samples in order of increasing scatter,  $\sigma_{int}$ . The panels of Figures (2) and (3) show the fitted plane in projection for all mentioned sub-classes. As we can see, going from the left to the right in Figure (2), the scatter decreases from the XRF to the long sample and it further decreases when we consider the planes shown in Figure (3) going from SEE to GRB-SNe ABC, and finally reaching the smallest scatter in the right panel with the gold sample. These planes also show that the GRB-SNe ABC category, which is strongly associated with SNe, are better correlated than that of the total GRB-SNe sample. This confirms a previous study performed in a 2D parameter space using the  $L_a - T_a^*$  correlation.

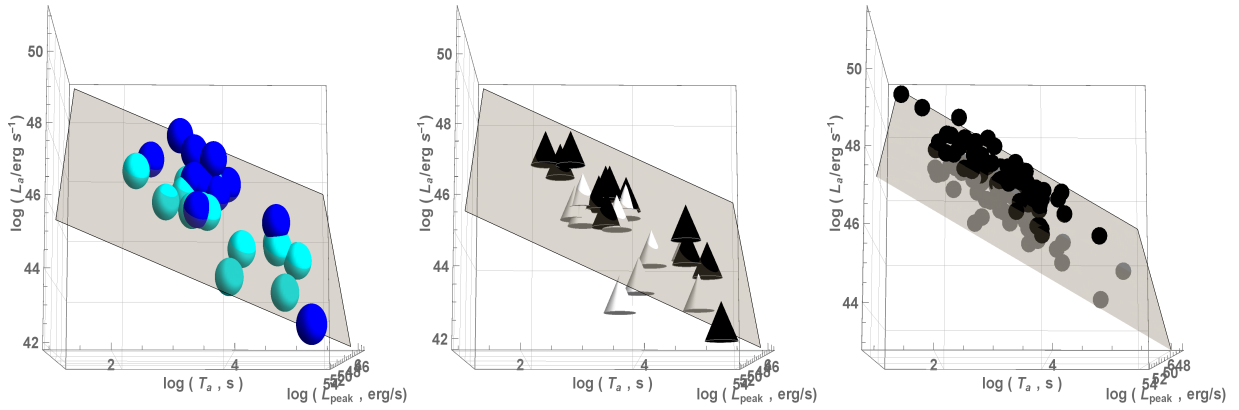


Fig. 2.— Projection of the  $(L_a, T_a, L_{peak})$  relation, in order of decreasing intrinsic scatter, for XRF, GRB associated with SNe, and long GRB respectively.

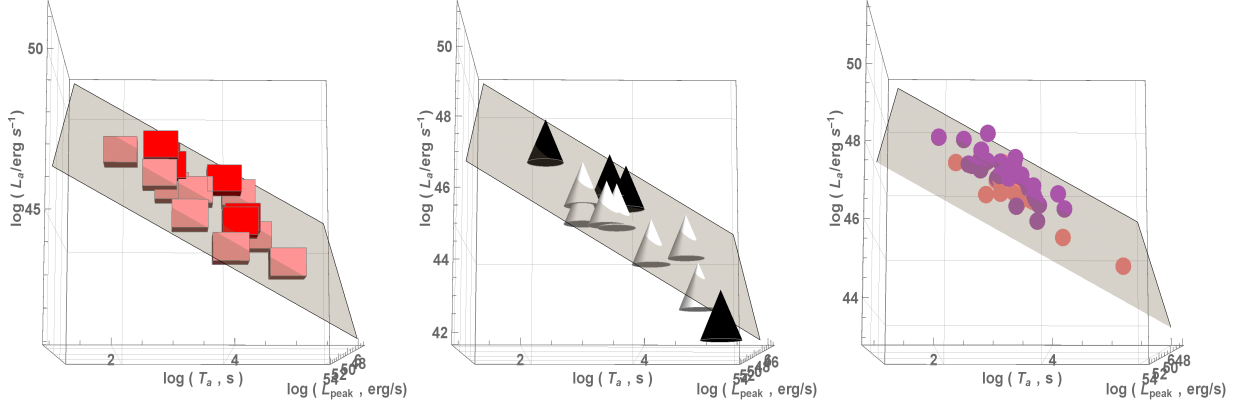


Fig. 3.— Projection of the  $(L_a, T_a, L_{peak})$  relation, in order of decreasing intrinsic scatter, for SEE, GRBs spectroscopically associated with SNe, and the gold sample respectively.

There are a few key details to notice in Table (1). Crucially, the gold sample still has the lowest intrinsic scatter of all the fitted categories. Another significant feature is that all of the plane parameters are within  $1\sigma$  of the fundamental plane set by the gold sample. The planes of these categories are not statistically different, thus we cannot hypothesize that these planes suggest different energy mechanisms, but we can conclude that the existence of the fundamental plane is confirmed to be driven by the gold sample features rather than the category based sampling. The one exception to the above is the case of the short GRBs with extended emission, the SEE category. Although from the distance to the plane of any particular GRB it is not possible to assign it to this category or another, the full SEE sample of 15 bursts has a mean distance to the gold plane of 0.56 (see figure 4). The above implies a z-score of  $-8.3$  for this sample <sup>8</sup>, and hence a probability of  $10^{-5}$  that the same z-score test statistic could be obtained by chance for the same population. Thus, we can conclude that SEE GRBs are in all likelihood produced by a distinct physical mechanism. SEEs may be related to short bursts and hence come from a different progenitor.

<sup>8</sup>The probability that a sub sample of  $n$  members drawn from an underlying gaussian distribution having a dispersion of  $\sigma$  will have a mean further away from that of the underlying distribution by more than  $X\sigma$ , will be determined by the probability corresponding to a z-score of  $(\sqrt{n}X)/\sigma$ .

Category	z-score	N
Gold	0.0	45
Long	-3.5	132
SNe	-5.8	22
XRF	-6.0	27
SEE	-8.3	15

Table 2: Table of z-scores for each subsample.

It can also be shown that no category distribution is significantly separated from the fundamental plane. In Figure (4), combined plots of the distribution of GRB geometric distance from the fundamental plane set by the gold sample are shown for each category. The fitting of the plane and the dispersion have been performed simultaneously to avoid fitting bias. Thus, the shift visible in Fig. 4 derives from the fact that the reference plane is the gold sample fundamental plane rather than each plane for each category. Indeed, the gold fundamental plane is placed in 0, as a reference plane. The center of the distributions for all of the GRB sub-categories lie within  $1\sigma_{int}$  of the gold fundamental plane. Again, the exception being the SEE class, which is seen to peak at a point where the gold sample has already fallen to very close to 0. In addition, as it is visible from the right panel of Fig. 4, where the probability distribution of smoothed histograms are plotted, the distance of the peaks of the distribution between the gold sample and the SSE is the largest. For details about the definition and how the smoothed histogram has been computed see Appendix 3. This strengthens the possibility that the distance to the plane for the gold sample is a relevant discriminant between GRB categories. Of note is the fact that the ultra-long GRBs can be associated with the fundamental plane. One possibility that could explain this is discussed in Greiner et al. (2015) where was found that an ultra-long GRB (GRB 111209A) was associated with a SNe, which may indicate a magnetar origin. There are only two ultra-long GRBs in this sample, so a full analysis of this type will have to wait until a larger sample is available.

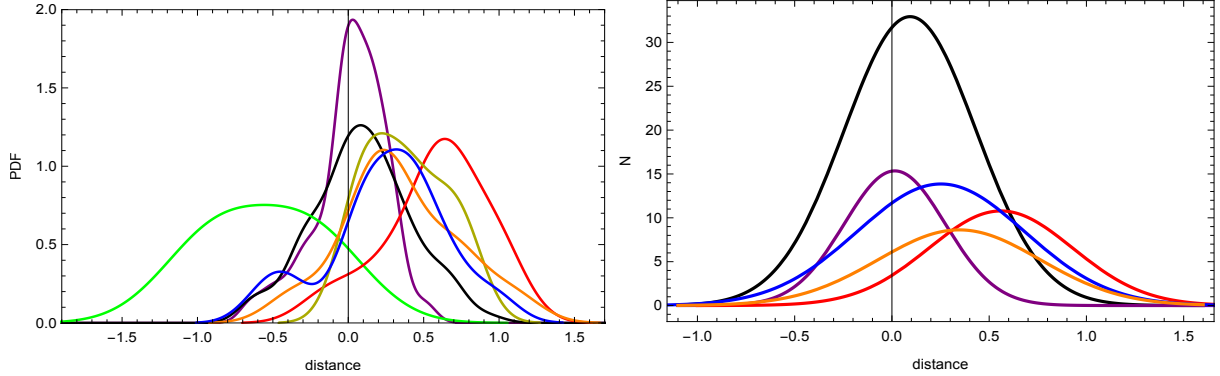


Fig. 4.— Left: A smoothed histogram showing the probability distribution function (PDF) of the distance distribution from the fundamental plane for GRBs of each category, including GRB-SNe (orange), GRBs spectroscopically associated with SNe (yellow), XRF (blue), SEE (red), gold sample GRBs (purple), long GRBs (black), and ultra-long GRBs (green). Right: A plot showing Gaussian fits of the distributions displayed in the left panel, using the same color scheme. A line perpendicular to  $x = 0$  is shown as the reference of the gold sample compared to the other categories. Ultra-long GRBs and GRBs spectroscopically associated with SNe are not shown as they had too little data to reliably fit them.

In a further attempt to reduce the scatter of the correlation we consider the rest frame time  $T_a^*$  as the dependent variable. This means that the length of the plateau depends on the peak luminosity and the luminosity at the end of the plateau itself. This choice is motivated not only from a mere hunt for a smaller scatter of the correlation, but it is also dictated by the intrinsic physics, since the length of the plateau in the magnetar model scenario is determined by the luminosity at the same time. Thus, it can be derived from fundamental physics, under this particular model, see Rowlinson et al. (2014) for details about this derivation. We present the results of this fitting in Table 3. Analogous to Table 1 we report the various GRB categories. The equation for the plane in this case is written in the following way:

$$\log T_a = C'_o + a' \times \log L_a + b' \times \log L_{peak} \quad (9)$$

Category	$C'_o$	$a'$	$b'$	$\sigma'_{int}$	N	$\Delta_\sigma$
SNe ABC	$21.13 \pm 5.85$	$-0.79 \pm 0.15$	$0.38 \pm 0.10$	$0.29 \pm 0.07$	11	12%
Gold	$24.15 \pm 6.79$	$-0.75 \pm 0.11$	$0.29 \pm 0.10$	$0.30 \pm 0.04$	45	6%
SEE	$16.73 \pm 7.45$	$-0.72 \pm 0.15$	$0.39 \pm 0.12$	$0.31 \pm 0.08$	15	21%
Long	$19.16 \pm 4.18$	$-0.69 \pm 0.07$	$0.33 \pm 0.06$	$0.38 \pm 0.03$	132	24%
SNe Total	$18.35 \pm 7.38$	$-0.74 \pm 0.17$	$0.39 \pm 0.12$	$0.48 \pm 0.08$	22	4%
XRF	$20.02 \pm 8.23$	$-0.58 \pm 0.16$	$0.22 \pm 0.12$	$0.48 \pm 0.07$	27	9%

Table 3: Table of best-fit values for relation plane parameters in order of increasing scatter,  $\sigma_{int}$ . The last column  $\Delta_\sigma$  indicates the difference in percentage about the computation using rest frame time,  $T_a$ , as the dependent variable.

We here note that the scatter of the relations considered with  $T_a$  as a dependent variable are smaller than the ones with  $L_a$ , at least more than 4% in the case of the GRB-SNe and reaching a 24% reduction for the total long sample category as it is indicated in the last column of Table 3. Thus, this new approach constitutes an improvement compared to the previous analysis especially for the long GRBs. We also checked that the fitting method used is not sensitive to scale differences between the dependent variables, thus we present in Table 4 the time  $T_a$  standardized to a central value of  $10^3$ s or normalized to the smallest value before the fitting. We note that the best fit parameters are compatible within  $1\sigma$  with the values presented in Table 3.

Category	$C'_o$	$a'$	$b'$	$\sigma_{int}$	$\Delta_\sigma$
Gold Normalized	$21.91 \pm 6.58$	$-0.74 \pm 0.10$	$0.29 \pm 0.09$	$0.30 \pm 0.04$	6%
Gold Standardized	$21.08 \pm 6.67$	$-0.75 \pm 0.11$	$0.29 \pm 0.09$	$0.30 \pm 0.04$	6%

Table 4: Table of best-fit values for relation plane parameters using the gold sample where the dependent variable  $T_a$  is either normalized or standardized. We note that there is not a significant change in the scatter,  $\sigma_{int}$ , from that of the gold sample in Table 3, showing that the fitting method used is not sensitive to scale differences.

A reduction in the scatter might allow us to employ the 3D gold fundamental plane relation, in combination with other GRB relations, as cosmological tools. This may be possible based on a previous study of some of us (Cardone et al. 2009) that showed that adding the 2D Dainotti relation,  $L_X - T_a^*$ , to other 5 GRB relations reduces the resulting confidence intervals on the inferred distance moduli by 14%. The sample of the Dainotti relation used in Cardone et al. (2009) was composed of only 28 GRBs vs the 45 GRBs presented here. The  $\sigma_{int}$  scatter of the 2D relation was  $\sigma_{int} = 0.33$  vs  $\sigma_{int} = 0.30$  of the

current 3D relation. Thus, this increase in the sample size and 10% decrease in the  $\sigma_{int}$  possibly allow a reduction in the inferred cosmological parameters if we replace the 2D Dainotti relation with the current 3D gold fundamental plane together with the other 5 GRB relations used in Schaefer et al. (2007).

We here note that the gold fundamental plane reaches a much smaller intrinsic scatter than the gold sample obtained with  $L_{peak}$  computed using the full BAT-Swift GRBs. We have a reduction of the scatter of 27%, while the results of the long sample for the GBM are comparable within  $1\sigma$  with the previous Swift results. This is a possible step forward in the use of the fundamental plane as a cosmological tool.

As previously noted in the introduction, the plane is confirmed also for GRBs observed by the Fermi-GBM. We have a sample of 47 GRBs which are in common among the sample observed by Swift and the sample observed by the GBM. We here present Table 5 that summarizes the results of the fitting for the long category using either the Fermi or Swift data by using  $L_{peak}$  in  $\text{erg s}^{-1}$ . As shown in the table, the normalization coefficient found using Fermi data is larger than the normalization coefficient found using the Swift data. This is expected given GBM’s larger energy band. We will not present the other categories due to the paucity of the data. From the table of Swift and GBM we can see that using the same GRB set, but with different spectral model for the prompt emission does not significantly alter results. As expected we have a change in the normalization, and consistent plane orientations confirming the physical nature of the 3D plane.

Category	$C_o$	$a$	$b$	$\sigma_{int}$	N
Long (Fermi)	$21.34 \pm 5.96$	$-0.89 \pm 0.07$	$0.58 \pm 0.10$	$0.43 \pm 0.07$	34
Long (Swift)	$17.22 \pm 7.50$	$-0.88 \pm 0.09$	$0.65 \pm 0.13$	$0.48 \pm 0.07$	34

Table 5: Table of best-fit values for relation plane parameters in order of increasing scatter,  $\sigma_{int}$ . These values are computed assuming 1024 ms.

#### 4. Independence of the Fundamental Plane from Selected Parameters

With the goal of further reducing the scatter of this 3D relation, a number of independent GRB parameters were tested to see whether or not a 4D relation existed that would significantly decrease the scatter of the fundamental plane. The tested quantities included  $T_{90}^*$ ,  $E_{peak}^*$ ,  $\alpha$ , and  $\theta_{jet}$ , the first two rest frame quantities.

We here check the dependence on the jet opening angle, but we will not discuss comparisons with several methods of computing this angle since it would be far beyond the scope

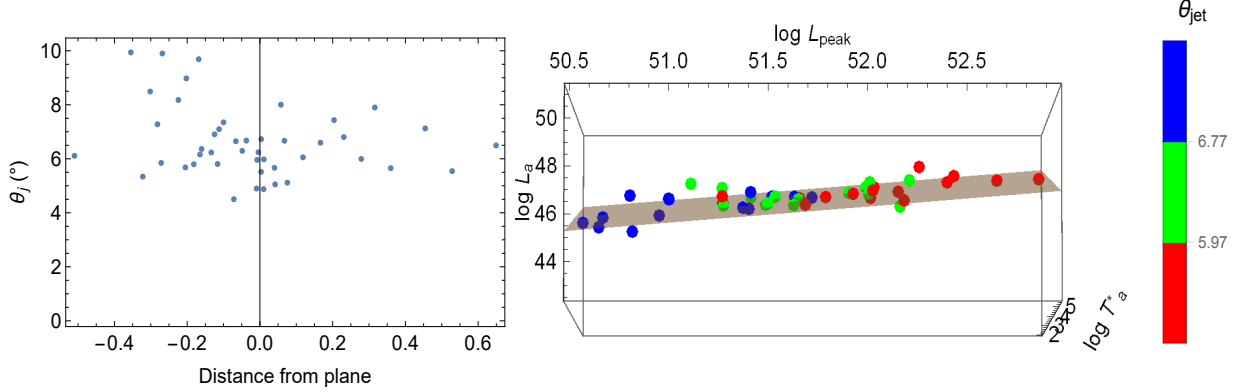


Fig. 5.— Left: A 2D plot of  $\theta_{jet}$  over distance from the fundamental plane for the gold sample. Right: Color bar plot of fundamental plane with a color bar depending on  $\theta_{jet}$ .

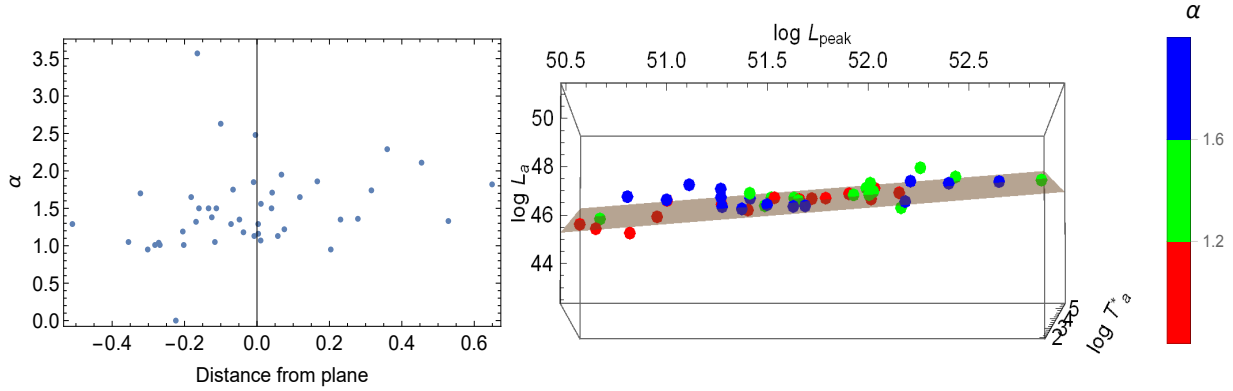


Fig. 6.— Left: A 2D plot of  $\alpha$  over distance from the fundamental plane for the gold sample. Right: Color bar plot of fundamental plane with a color bar depending on  $\alpha$ .

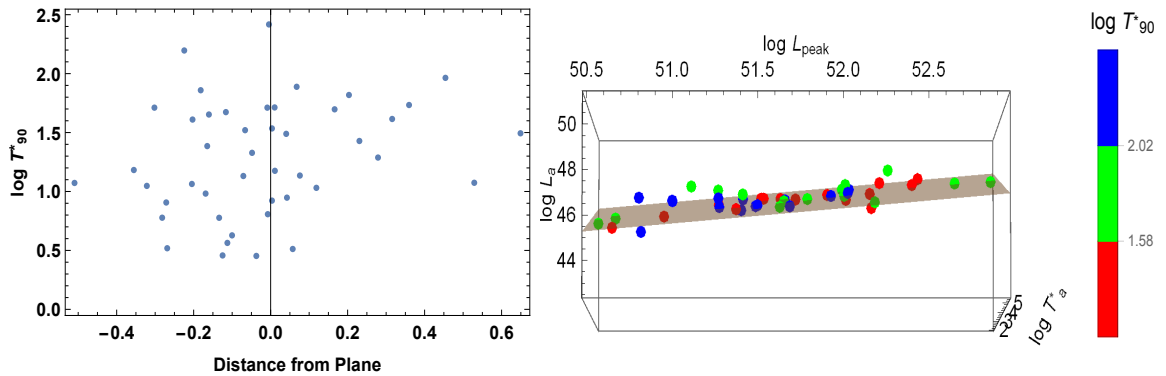


Fig. 7.— Left: A 2D plot of  $T_{90}^*$  over distance from the fundamental plane for the gold sample. Right: Color bar plot of fundamental plane with a color bar depending on  $T_{90}^*$ .

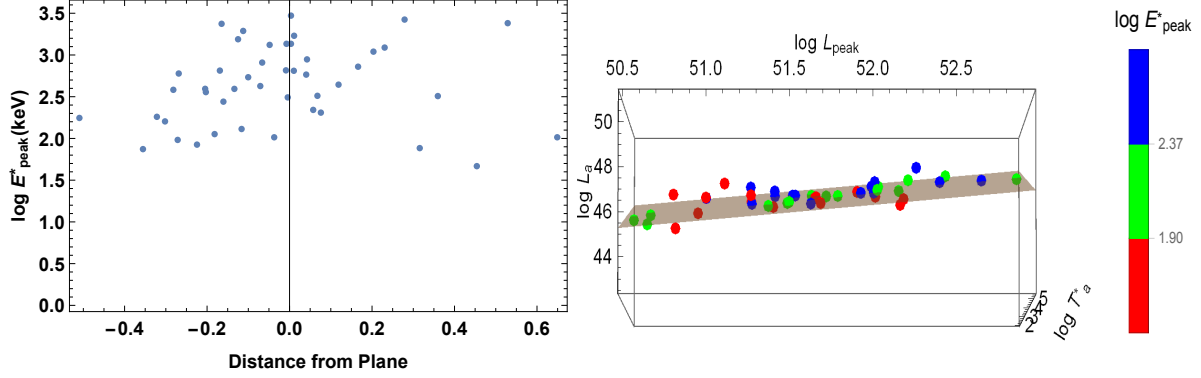


Fig. 8.— Left: A 2D plot of  $E^*_{\text{peak}}$  and the distance from the fundamental plane for the gold sample. Right: Color bar plot of fundamental plane with a color bar depending on  $E^*_{\text{peak}}$ .

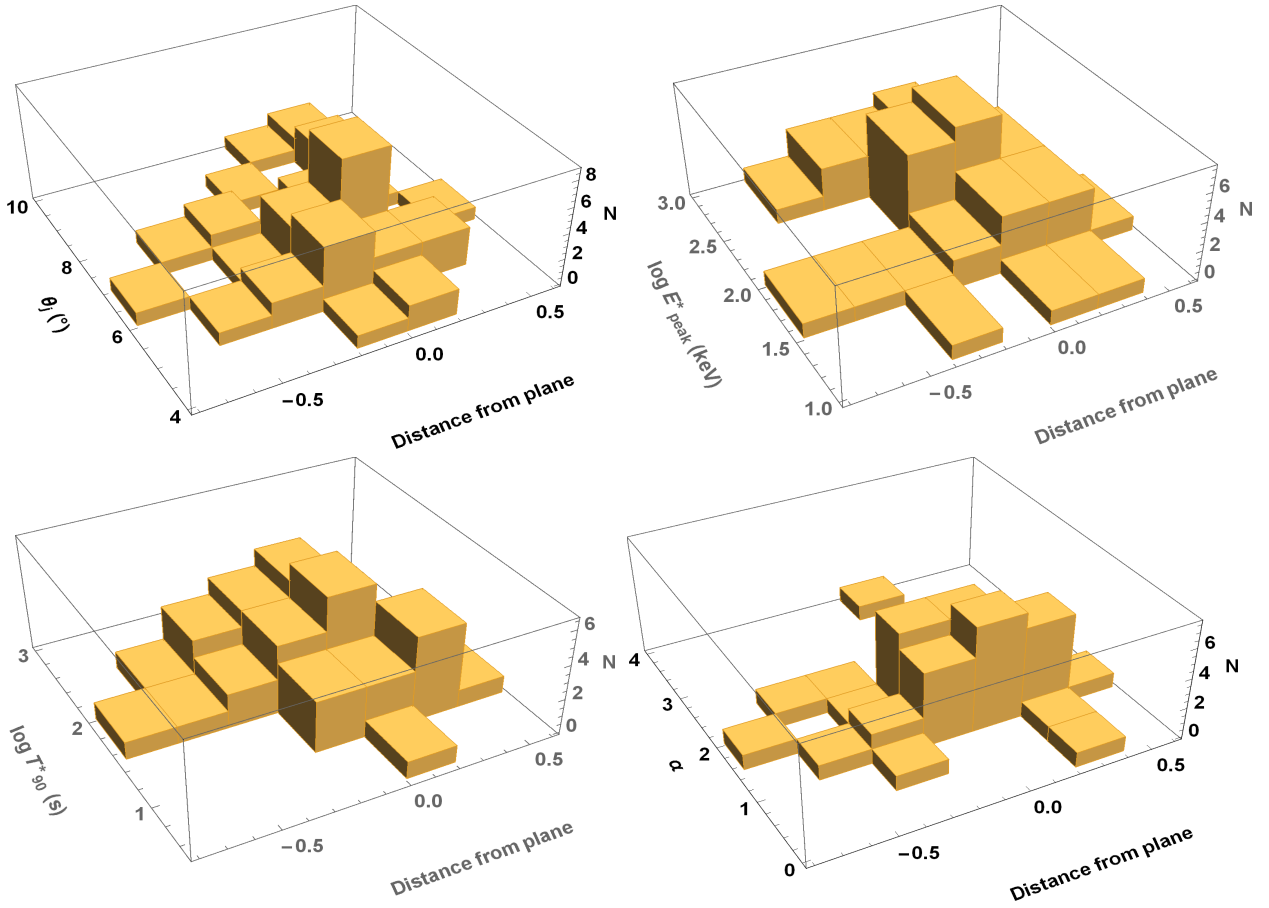


Fig. 9.— 3D histograms of the relationship between the same prompt and afterglow parameters of Figures (5)-(8) and the geometric distance from the fundamental plane.

of the paper. For details on how we estimate the jet opening angle see the Appendix 1.

On the left panels of Figures (5)-(8), there are plots of these parameters versus the geometric distance to the fundamental plane derived from the gold sample. On the right panel of the same figures, the four-dimensional color bar plots visually show the relationship between the parameters and the positions of the points on the plane. If a correlation had existed between the parameters and the plane, a clear pattern should have been seen in the scatter and color bar plots. There are no explicit trends in the scatter plots or groupings of colors shown. The Spearman coefficient for these distributions is uniformly  $\leq 0.40$ , confirming the lack of real correlation for these parameters.<sup>9</sup> We here note that since the Yonetoku-relation is between  $E_{peak}$  and  $L_{peak}$  in the prompt emission, one could expect a correlation between  $E_{peak}$  and the fundamental plane. However, this is a 3-parameter correlation, thus while the contribution to this correlation is high for the presence of  $L_{peak}$ , it diminishes when we consider the correlation between  $E_{peak}$  and  $(L_a, T_a)$ . The Spearman and Pearson correlation coefficients for each of the parameters versus the geometric distance from the fundamental plane is given in Table (6).

Parameter	Spearman $\rho$	$R^2_{adj}$	R	Probability
$\alpha$	0.40	0.05	0.26	0.04
$\theta_{jet}$	0.21	0.03	0.23	0.06
$\log T_{90}^*$	0.26	0.02	0.22	0.08
$\log E_{peak}^*$	0.30	0.02	0.20	0.09

Table 6: Statistical and correlation parameters for linear fits of the parameters versus geometric distance from the fundamental plane.

In order to visually inspect these relations further, we plot 3D histograms of the parameters and distance from the plane in Figure (10). These plots strengthen the conclusion that there is no underlying relationship between the studied variables. This outcome reinforces the previous result that the fundamental plane is independent from the prompt and afterglow emission parameters tested.

---

<sup>9</sup>The Spearman coefficient is a nonparametric measure of rank correlation. A Spearman coefficient less than 0.50 generally means that the correlation is not meaningful.

## 5. Conclusions

In our investigation of GRB sub-classes, we confirmed the results of Dainotti et al. (2016). Plateau phase GRBs can be used to isolate a sub-class of events that define a very tight plane in a three-dimensional space of  $(\log L_a, \log T_a, \log L_{peak})$ . We confirm that the scatter about this 3D plane is still the smallest when the gold sample, a specific class of GRBs without steep plateaus and with good coverage of the data, is used for the fitting. The previous gold sample was extended to contain pertinent events up to July 2016, for a total of 45 events, and an updated fundamental plane was found with an intrinsic scatter compatible within one  $\sigma$  with the previous finding. All other tested relation planes related to the different categories have a larger intrinsic scatter than the fundamental plane derived from the gold sample. We find that the relation planes for each of the mentioned categories are not statistically different from the plane derived from the gold sample, with the exception of the SEE, which are hence identified as a physically distinct class of objects. Thus, the distance of any particular GRB category from this plane becomes a key parameter, as it can be used as a discriminant feature among long GRBs and the SEE.

In addition, we confirmed this 3D relations by using GRBs observed at high energy, namely by computing the  $L_{peak}$  values derived from the Fermi-GBM, thus showing that the relation is independent of the energy range. The gold fundamental plane obtained with the GBM data presents an intrinsic scatter which is 27% smaller than the gold sample with the Swift data thus further confirming the existence of this 3D relation. Furthermore, we computed the several category planes by using  $T_a$  as a dependent parameter obtaining for each category smaller intrinsic scatters (reaching a reduction of 24% for all the long GRBs). In order to gain insight into the robustness of the fundamental plane, we explored possible dependencies on a variety of fourth parameters. We found no significant such 4D relations when considering several relevant prompt and afterglow parameters, namely  $\alpha$ ,  $T_{90}^*$ ,  $E_{peak}^*$  and  $\theta_{jet}$ , using the  $E_{iso} - E_\gamma$  relation of the method in Pescalli et al. (2015). Given the approximately inverse relation between  $T_a^*$  and  $L_{peak}$  in the afterglow parameters, the plane obtained suggests to first order, a strong energy coupling between the afterglow phase (of total energy  $E_{aft} \approx T_a^* L_{peak}$ ) and the prompt  $L_{peak}$  of the type  $E_{aft} \propto L_{peak}^{2/3}$ , given the coefficient of  $L_{peak}$  in the plane relation of  $b = 0.64 \pm 0.11$ . This energy coupling would favour intrinsic progenitor based GRB afterglow models over explanations based on external environmental properties. However, previous studies (Del Vecchio et al. 2016) have shown that there is a dependence of  $\alpha$  on the  $L_a - T_a^*$  relation, which indeed disappears when we consider 4D correlation. In consistency with the above, we found no significant relation of  $\alpha$  as a fourth parameter. The careful inference of GRB opening angles and their relevance to the 3D correlation between lightcurve physical parameters explored here is clearly a desirable extension.

## 6. Acknowledgments

This work made use of data supplied by the UK Swift Science Data Centre at the University of Leicester. We are particularly grateful to M. Ostrowski and L. Amati for his relevant comments and suggestions which helped improving the manuscript. We are thankful to C. Gilberson for his initial contribution to the manuscript during his summer internship at SLAC in 2016. S. S. acknowledges the Department of Energy of US to support her summer internship (SULI program) and the Department of Physics of Stanford University for hosting her. M.G.D acknowledges the Marie Curie Program, because the research leading to these results has received funding from the European Union Seventh Framework Program (FP7-2007/2013) under grant agreement N 626267. X.N. acknowledges support from UNAM DGAPA PAPIIT grant IN-104517. S.N. acknowledges the funding support of the JSPS, the Mitsubishi Foundation, Associate Chief Scientist Program of RIKEN, a RIKEN pioneering project ‘Interdisciplinary Theoretical Science (iTHES)’, and ‘Interdisciplinary Theoretical & Mathematical Science Program (iTHEMS)’ of RIKEN.

## A. Appendix 1

For simplicity the luminosity and energy output of GRBs are calculated assuming isotropic emission because the necessary quantity to account for the collimation of the emission, namely the jet opening angle, is very difficult to acquire without simultaneous multi-wavelength observations. While several methods have been used to obtain this angle (Ghirlanda et al. 2004; Goldstein et al. 2011; Lu et al. 2012; Fong et al. 2015), we do not have this estimate for all GRBs. Thus, in order to obtain estimates for  $\theta_{jet}$ , we turn to the method of Pescalli et al. (2015) in which the jet opening angle can be derived using the  $E_{peak} - E_{\gamma}$  relation (Ghirlanda et al. 2004) and the  $E_{peak} - E_{iso}$  (Amati et al. 2002). We use equation (8) of Pescalli et al. (2015), repeated below, to compute these angle values:

$$1 - \cos\theta_{jet} = \left(\frac{k_A}{k_G}\right)^{1/G} E_{iso}^{\frac{A-G}{G}} \quad (A1)$$

where  $k_A$  and  $k_G$  are the normalization constants, and  $A$  and  $G$  are the slopes of the Amati and Ghirlanda relations.

From Ghirlanda et al. (2004):

$$E_{peak} = k_G \times E_{\gamma}^G = 267 \times (E_{iso}(1 - \cos\theta_{jet})/(4.3 \times 10^{50} \text{erg}))^{0.706 \pm 0.047} \quad (A2)$$

From Amati et al. (2014):

$$\log E_{peak} = 0.52 \pm 0.06 \times \log(E_{iso}/10^{52} \text{erg}) + 2 \quad (A3)$$

or

$$E_{peak} = k_A \times E_{iso}^A = 100 \times (E_{iso}/10^{52} \text{erg})^{0.52 \pm 0.06} \quad (\text{A4})$$

By equating and simplifying these equations, one gets the following:

$$1 - \cos\theta_{jet} \approx \frac{5.36 \times 10^{11}}{E_{iso}^{0.26}} \quad (\text{A5})$$

Thus, an angle can be easily calculated for all GRBs with known  $E_{iso}$  values. These values of  $\theta_{jet}$  are computed in the current paper. However, we here stress that this estimation is rough. In fact, to effectively and properly use the Amati and Ghirlanda relations to estimate the jet opening angle, the distribution of the scatter must be taken into account, as well as the correlation between the two relations themselves since they both rely on the same  $E_{peak}$  values. However, here we use this first order approach in a first attempt to investigate if a dependence on the angle is present.

## B. Appendix 2

When creating the gold sample, we required that the angle of the plateau be less than  $41^\circ$  because the distribution of the angles shown in Fig. 10 present a tail (marked in violet colour) above  $41^\circ$ . Indeed, if we remove this tail we are able to fit the distribution with a gaussian centered around  $25^\circ$ . We also note that this cut excludes only 9% of the total distribution. This result is compatible with the cut on the previous sample which excluded the 11% of the data sample.

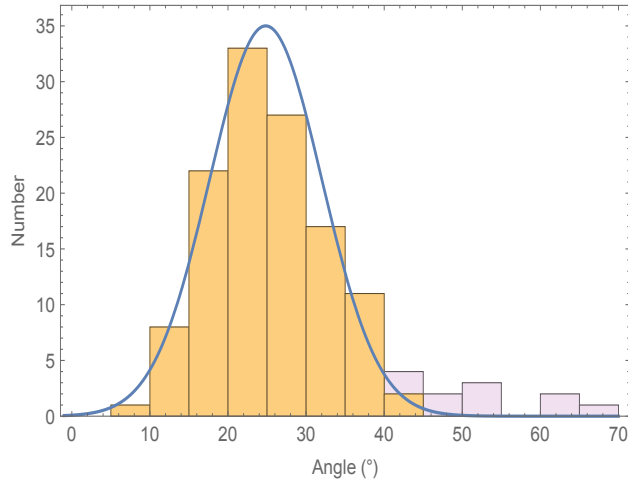


Fig. 10.— Distribution of the plateau angles. Orange represents the GRBs whose plateau angle is within the  $41^\circ$  requirement.

### C. Appendix 3

The smoothed histogram are based on a smooth kernel density estimate computed with Mathematica 11.1 with a default build-in option that allow for an automatic bandwidth. More specifically, the probability density function for SmoothKernelDistribution for a value  $x$  is given by a linearly interpolated version of for a smoothing kernel  $k(x)$  and bandwidth parameter  $h$  of the form :

$$1/nh \sum_{i=1}^n k\left(\frac{x - x_i}{h}\right) \quad (C1)$$

By default the Gaussian kernel is used.

## REFERENCES

Amati L., Frontera F., Tavani M. et al. 2002, A&A, 390, 81

Amati, L. et al. 2009, A&A, 508, 173.

Amati, L. et al. 2014, ANNALEN DER PHYSIK, 526, 340.

Avni, Y. 1976, ApJ, 210, 642

Bernardini, M.G. et al. 2012, A&A, 539, 3.

Blustin, A. J., Band, D., Barthelmy, S., et al. 2006, ApJ, 637, 901

Burrows, D. N., Grupe, D., Capalbi, M., et al. 2006, ApJ, 653, 468

Cardone, V.F. et al. 2009, MNRAS, 400, 775.

Cardone, V.F., et al. 2010, MNRAS, 408, 1181.

Cannizzo, J. K. & Gehrels, N., 2009, ApJ, 700, 1047.

Cannizzo, J. K., et al. 2011, ApJ, 734, 35.

Cenko, S. B., Kasliwal, M., Harrison, F. A., et al. 2006, ApJ, 652, 490

Cenko, S. B., et al. 2010, ApJ, 711, 641

Chandra, P., et al. 2010, ApJ, 712, L31

Collazzi, A. C., & Schaefer, B. E. 2008 ApJ, 688, 456.

Cucchiara, N. et al. 2011, ApJ, 736, 7.

Curran, P. A., van der Horst, A. J., Beardmore, A. P., et al. 2007, A&A, 467, 1049

D' Agostini, G. 2005, arXiv:physics/0511182

Dall'Osso, S. et al. 2011, A&A, 526A, 121D

Dai, X. et al. 2007, ApJ, 658, 509

Dainotti, M. G. et al. 2008, MNRAS 391L, 79.

Dainotti, M.G. et al. 2010, ApJL, 722, L215.

Dainotti, M. G. et al. 2011a, ApJ, 730, 135.

Dainotti, M.G. et al. 2011b, MNRAS, 418, 2202.

Dainotti, M.G., et al. 2013, ApJ, 774, 157.

Dainotti, M.G., et al. 2013b, MNRAS, 436, 82.

Dainotti, M.G., et al. 2015a, ApJ, 800, 31.

Dainotti, M.G., et al. 2015b, MNRAS, 451, 4.

Dainotti, M.G., et al. 2016, ApJL, 825, L20.

el Vecchio, R., Dainotti, M.G. & Ostrowski, M., ApJ 2016, 828, 36

De Pasquale, M., Beardmore, A. P., Barthelmy, S. D., et al. 2006, MNRAS, 365, 1031

Efron, B. & Petrosian, V., 1992, ApJ, 399, 345.

Enderli, M., et al. 2016, ArXiv e-prints

Evans, P. A., et al. 2009, MNRAS, 397, 1177

Ferrero, P., Klose, S., Kann, D. A., et al. 2009, A&A, 497, 729

Fong, W., et al. 2014, ApJ, 780, 118

Fong, W., et al. 2015, ApJ, 815, 102F.

Frail D.A. et al. 2006, ApJ, 646, L99

Gerhels, N. et al. 2004, ApJ, 611, 1005.

Ghirlanda, G., et al. 2004, *ApJ*, 616, 331.

Ghirlanda G., Nava L., Ghisellini G., Firmani C., 2007, *A&A*, 466, 127

Ghisellini, G., et al. 2008, *A&A*, 496, 3, 2009.

Goldstein, A., et al. 2016, *ApJ*, 818, 18.

Greiner, J., Mazzali, P. A., Kann, D. A., et al. 2015, *Nature*, 523, 189

Grupe, D., Brown, P. J., Cummings, J., et al. 2006, *ApJ*, 645, 464

Grupe, D., et al. 2007, *ApJ*, 662, 443

Grupe, D., et al. 2010, *ApJ*, 711, 1008

Guidorzi, C., Mundell, C. G., Harrison, R., et al. 2014, *MNRAS*, 438, 752

Hjorth, J., & Bloom, J.S, 2011, ‘Gamma-Ray Bursts’, eds. C. Kouveliotou, R. A. M. J. Wijers, S. E. Woosley, Cambridge University Press, 2011.

Hurkett, C. P. et al. 2006, *MNRAS*, 368, 1101

Izzo, et al. 2015, *A&A*, 582A, 115.

Jia, L. W. et al. 2012, *RAA*, 12, 411

Kamble, A., Misra, K., Bhattacharya, D., et al. 2009, *MNRAS*, 394, 214

Kouveliotou, C., et al. 1993, *ApJ*, 413, L101.

Kumar, P. & Panaiteescu, A., 2008, *MNRAS*, 391, L19

Laskar, T., Berger, E., Tanvir, N., et al. 2014, *ApJ*, 781, 1

Laskar, T., Berger, E., Margutti, R., et al. 2015, *ApJ*, 814, 1

Levan, A. J., et al. 2007, *MNRAS*, 378, 1439

Lloyd, N., & Petrosian, V. *ApJ*, 1999, 511, 550.

Lu, R., et al. 2012, *ApJ*, 745, 168.

Marshall, F. E., Antonelli, L. A., Burrows, D. N., et al. 2011, *ApJ*, 727, 132.

Mazets, E. P. et al. 1981, *Astrophys. Space Sci.*, 1981, 80, 3.

Mundell, C. G., et al. 2007, *ApJ*, 660, 489

Nakauchi D., Kashiyama K., Suwa Y., Nakamura T., 2013, *ApJ*, 778, 67

Nappo, F., Pescalli, A., Oganesyan, G., et al. 2016, arXiv:1604.08204

Nicuesa Guelbenzu, A., Klose, S., Rossi, A., et al. 2011, *A&A*, 531, L6

Nicuesa Guelbenzu, A., Klose, S., Greiner, J., et al. 2012, *A&A*, 548, A101

Norris, J.P & Bonnell, J.T. 2006, *ApJ*, 643, 266.

Norris, J.P., Gehrels, N. & Scargle, J. 2010, *ApJ*, 717, 411.

O' Brien, P.T., Willingale, R., Osborne, J. et al. 2006, *ApJ*, 647, 1213.

Oates, S. R., de Pasquale, M., Page, M. J. et al. 2007, *MNRAS*, 380, 270

Oates, S. R. et al. 2012, *MNRAS*, 426L, 86.

Perri, M., et al. 2005, *A&A*, 442, L1

Perri, M., Guetta, D., Antonelli, L. A., et al. 2007, *A&A*, 471, 83

Piro, L. et al. 2014, *ApJ*, 790L, 15.

Pescalli, A., et al. 2015, *MNRAS*, 447, 1911

Postnikov, S., et al. 2014, *ApJ*, 783, 126.

Qi, S., Lu, T., & Wang, F.-Y., 2009, *MNRAS*, 398, L78

Rea, N . et al. 2015, *ApJ* 813, 92.

Rossi, A., Schulze, S., Klose, S., et al. 2011, *A&A*, 529, A142

Rowlinson, A. et al. 2013, *MNRAS*, 430, 1061.

Rowlinson, A. et al. 2014, *MNRAS*, 443, 1779.

Sakamoto, T. et al. 2011, *ApJS*, 195, 2.

Schaefer, B. 2007, *ApJ*, 660, 16.

Shao, L. & Dai, Z. G. 2007, *ApJ*, 660, 1319.

Soderberg, A. M., et al. 2006, *ApJ*, 650, 261

Soderberg, A. M., et al. 2007, *ApJ*, 661, 982

Sollerman, J., Fynbo, J. P. U., Gorosabel, J., et al. 2007, *A&A*, 466, 839

Starling, R. L. C., Rol, E., van der Horst, A. J., et al. 2009, *MNRAS*, 400, 90

Stratta, G. et al. 2007, *A&A*, 474, 827

Toma, K., Ioka, K., Sakamoto, T., & Nakamura, T. 2007, *ApJ*, 659, 1420

Troja, E. et al. 2007, *ApJ*, 665, 599

Troja, E. et al. 2016a, *ApJ*, 827, 102T

Troja E., et al., 2016b, preprint

Tsutsui, R., et al. 2009, *JCAP*, 08, 015.

Vaughan, S., et al. 2005, *ApJ* 638, 920

Wang, Y et al. 2016, 818,167

Willingale, R. W. et al., *ApJ*, 2007, 662, 1093.

Willingale, R. et al. 2010, *MNRAS*, 403, 1296.

Wózniak, P. R., Vestrand, W. T., Panaitescu, A. D., Wren, J. A., Davis, H. R., and White, R. R. 2009, *ApJ*, 691, 495

Xiao, L. & Schaefer, B.E. 2009, *ApJ*, 707, 387.

Xu, M., Huang, Y.-F. & Lu, T., 2009, *RAA*, 9, 1317

M. Xu & Y. F. Huang, *A&A* 2012, 538, 134.

Yonetoku, D. et al. 2004, *ApJ*, 609, 935.

Zhang, B & Mészáros, P. 2001, *ApJ*, 552L, 35.